HHS Public Access

Author manuscript

Cell Rep. Author manuscript; available in PMC 2023 October 23.

Published in final edited form as:

Cell Rep. 2023 February 28; 42(2): 112039. doi:10.1016/j.celrep.2023.112039.

Circadian regulation of dentate gyrus excitability mediated by G-protein signaling

Jose Carlos Gonzalez[1], **Haeun Lee**[1], **Angela M. Vincent**[1], **Angela L. Hill**[1], **Lacy K. Goode**[2], **Gwendalyn D. King**[3], **Karen L. Gamble**[2], **Jacques I. Wadiche**[1,*], **Linda Overstreet-Wadiche**[1,4,*]

[1]Department of Neurobiology and McKnight Brain Institute, University of Alabama at Birmingham, Birmingham, AL 35294, USA

[2]Department of Psychiatry and Behavioral Neurobiology, University of Alabama at Birmingham, Birmingham, AL 35294, USA

[3]Department of Biology, Creighton University, Omaha, NE 68178, USA

[4]Lead contact

SUMMARY

The central circadian regulator within the suprachiasmatic nucleus transmits time of day information by a diurnal spiking rhythm driven by molecular clock genes controlling membrane excitability. Most brain regions, including the hippocampus, harbor similar intrinsic circadian transcriptional machinery, but whether these molecular programs generate oscillations of membrane properties is unclear. Here, we show that intrinsic excitability of mouse dentate granule neurons exhibits a 24-h oscillation that controls spiking probability. Diurnal changes in excitability are mediated by antiphase G-protein regulation of potassium and sodium currents that reduce excitability during the Light phase. Disruption of the circadian transcriptional machinery by conditional deletion of *Bmal1* enhances excitability selectively during the Light phase by removing G-protein regulation. These results reveal that circadian transcriptional machinery regulates intrinsic excitability by coordinated regulation of ion channels by G-protein signaling, highlighting a potential novel mechanism of cell-autonomous oscillations.

Graphical abstract

*Correspondence: jwadiche@uab.edu (J.I.W.), lwadiche@uab.edu (L.O.-W.).

AUTHOR CONTRIBUTIONS

Conceptualization and Methodology, J.C.G. and L.O.-W.; Formal Analysis and Investigation, J.C.G., H. L., A.M.V., A.L.H., L.K.G, K.L.G., and L.O.-W.; Resources, G.D.K., K.L.G., J.I.W., and L.O.-W.; Writing-Original Draft, J.C.G. and L.O.-W.; Writing-Review and Editing, J.C.G., L.K.G., G.D.K., K.L.G., J.I.W., and L.O.-W.; Supervision and Project Administration, G.D.K., K.L.G., J.I.W., and L.O.-W.; Funding Acquisition, J.C.G., K.L.G., J.I.W., and L.O.-W.

DECLARATION OF INTERESTS

The authors declare no competing interests.

INCLUSION AND DIVERSITY

We support inclusive, diverse, and equitable conduct of research.

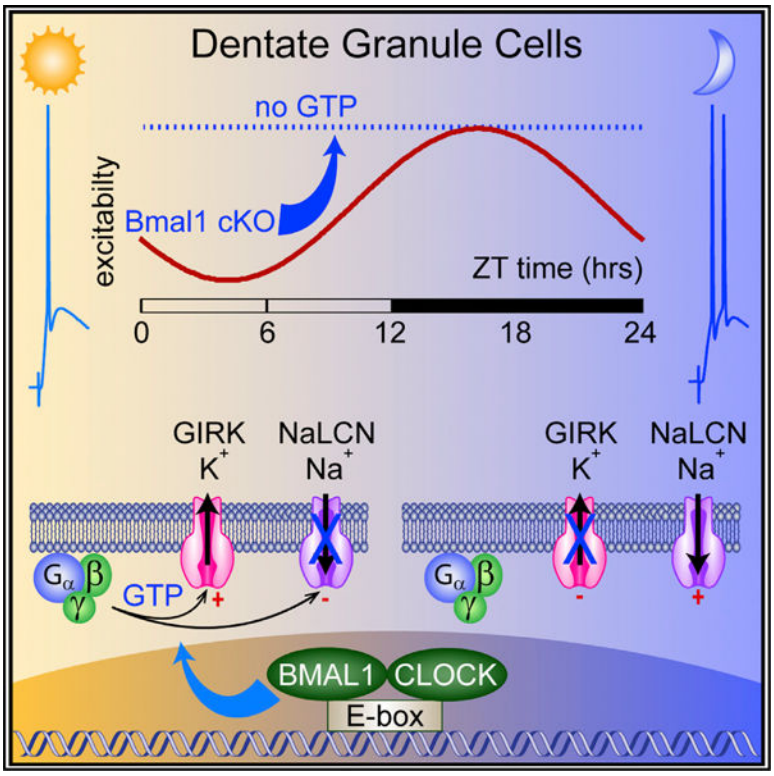

In brief

Gonzalez et al. show that dentate gyrus neurons exhibit a 24-h cycle of intrinsic excitability and synaptic recruitment mediated by inhibitory G-protein regulation of membrane currents. The cycle of excitability is linked to the cell-intrinsic molecular clock transcriptional machinery, with low excitability during the Light phase.

INTRODUCTION

The suprachiasmatic nucleus (SCN) is the primary pacemaker that governs daily rhythms by self-sustaining transcriptional-translational feedback loops that define a molecular clock.[1] These loops control the membrane excitability of SCN neurons, allowing it to transmit time of day information by an endogenous oscillation of spiking activity.[2] Similar transcriptional loops drive local circadian programs of clock-controlled output genes in the hippocampus that interact with sleep-wake cycles to drive daily regulation of the synaptic proteome.[3,4] While diurnal rhythms of synaptic function related to sleep-wake cycles are well-established,[5–7] it is unclear whether local transcriptional clocks in the hippocampus also affect membrane excitability. Addressing this question is important for understanding how disruption of clock components contributes to abnormal excitability and epilepsy, as well as the daily rhythms of normal behavior.[8–11]

A 24-h fluctuation of cortical-evoked population spikes and excitatory postsynaptic potentials (EPSPs) in the dentate gyrus (DG) of awake rats and squirrel monkeys provided early evidence for circadian regulation of hippocampal input-output transformations.[12] The

DG serves as a ‘‘gate’’ that filters incoming information from the entorhinal cortex to enable efficient information processing in CA3. The DG gate is maintained by the low propensity of the principal granule cells (GCs) to fire action potentials. GCs suppress propagation of neural activity through the cortico-hippocampal circuit by strong synaptic inhibition from local GABAergic interneurons.[13,14] Excitatory synaptic input related to dendritic complexity and differences in intrinsic excitability also contribute to the selection of GCs that comprise active ensembles.[15–17] Thus, both synaptic and intrinsic mechanisms could underlie time of day regulation of input-output transformations.

One intrinsic property that controls excitability is the membrane conductance that determines the resting membrane potential (RMP) and input resistance (IR). This membrane conductance is primarily set by leak K^+ and Na^+ channels, with a ratio that varies in a cell-type-specific manner. In GCs, G-protein coupled inwardly rectifying (GIRK) and other leak K^+ conductances provide low intrinsic excitability by hyperpolarization and low membrane resistance.[18–20] GCs also express NALCN, an Na^+ leak channel that is typically suppressed by extracellular Ca^{2+} and inhibitory G-protein signaling.[21,22] In central pacemaker neurons of flies and mice, molecular clock-controlled modulation of resting Na^+ and K^+ conductances are responsible for rhythms of membrane excitability that generate endogenous oscillations of spiking.[23–27] Here we show that G-protein signaling, a pathway with robust circadian transcription independent of sleep-wake cycles,[4] contributes to diurnal regulation of intrinsic excitability and synaptic recruitment in the DG.

RESULTS

Reduced recruitment of GCs during the Light phase compared with Dark phase

To compare excitability across the diurnal cycle, we prepared hippocampal slices during the Light phase (zeitgeber time, ZT 5.5 or 11.5 where ZT 12 refers to lights off) and performed recordings between projected ZT 8–11 (referred to as ‘‘Light phase’’) or ZT 14–17 (‘‘Dark phase’’). This schedule avoids potential photic interference in slices prepared during the Light and Dark phases. We recorded from visually identified GCs and stimulated the perforant path near the crest to minimize direct stimulation of local interneurons (Figure 1A). This paradigm reliably generated EPSPs at the lowest stimulus intensity but failed to recruit spikes during the Light phase, whereas up to ~40% of GCs were recruited to spike during the Dark phase (Figure 1B). We obtained similar results in GCs from different lines of transgenic mice (Figure S1). Thus, perforant path recruitment of GC spiking is robustly different across the diurnal phase, with lower excitability during the Light phase.

$GABA_A$ receptor-mediated inhibition strongly suppresses GC spiking.[13,28] Accordingly, gabazine (GBZ; 10 μM) increased the percent of spiking GCs during both the Light and Dark phases (Figure 1C, left, middle). But in GBZ, the percentage of GCs that spiked remained lower during the Light phase compared with the Dark phase (Figure 1C, right). Thus, diurnal changes in GABAergic inhibition cannot account for differential spiking. To address other mechanisms, we compared subthreshold EPSPs in GBZ. At low stimulus intensities, the maximum depolarization was lower during the Light than Dark and the difference vanished at higher stimulus intensities as threshold was reached, suggesting no difference in spike threshold (Figure 1D). There was no difference in the amplitude and rise

time of subthreshold EPSPs when measured from respective resting potentials (Figure S1). However, there was a pronounced difference in the time course of subthreshold EPSPs, with the half-width reduced during the Light phase, both in the absence and presence of GBZ (Figure 1E). Since the membrane time constant (TC) dictates the decay phase of EPSPs, these results suggest that differences in GC spiking probability across Light and Dark phases could result from changes in intrinsic excitability.

Reduced intrinsic excitability during the Light phase

To investigate intrinsic membrane properties, we bypassed synaptic stimulation and elicited action potential firing by current injections. During the Light phase, GCs exhibited lower propensity for spiking, illustrated by a rightward shift in the spike-current relationship compared with the Dark phase (Figure 2A). There was also a significant reduction in passive excitability during the Light phase, with a more hyperpolarized RMP (−75.5 ± 0.3 versus −70.6 ± 0.5 mV), lower IR (281 ± 8 versus 345 ± 13 MΩ), and faster membrane TC (27.8 ± 0.7 versus 34.2 ± 1.1 ms), culminating in higher rheobase, the current required to achieve threshold (66.1 ± 1.9 versus 50.7 ± 2.2 pA) (Figure 2B, violin plots). To assess whether these parameters varied systematically across the time of day, we pooled results from recordings in 1-h bins across 24 h (Figure 2B, dot plots). Cosinor analysis revealed significant rhythmicity of RMP, IR, TC, and rheobase (R^2 = 0.37, 0.17, 0.28, and 0.17, respectively). The mesor, amplitude, and acrophase values (Table S1) showed that the peak of GC excitability defined by acrophase values for rheobase occurred at ZT 16 (low rheobase) with the trough of excitability at ZT 4 (high rheobase) (Figure 2C).

Since the light-dark cycle entrains many physiological and behavioral rhythms,[29] we also measured GC intrinsic excitability in mice kept in constant darkness (DD). After 30 days of DD, we made acute slices during Subjective Night (active) or Subjective Day (inactive) phases and found that GCs still exhibited differential intrinsic excitability similar to the 12:12 L-D values. This was exemplified by rheobase (85.5 ± 3.8 pA for Subjective Day versus 61.8 ± 2.7 pA for Subjective Night; Figure 2D), as well as other measures of intrinsic excitability, including the number of action potentials elicited by current injection (Figure S2). Furthermore, GCs from both male and female mice showed reduced excitability during the Light and there was no interaction between sex and the recording window (Figure S2 and Table S2). Low excitability during the Light also did not depend on tonic $GABA_A$ receptor activity, since GBZ had minimal effects on intrinsic properties (Figure S2). Together these data show a daily rhythm of GC intrinsic excitability independent of $GABA_A$ receptor-mediated inhibition likely contributes to diurnal regulation of DG excitability *in vivo*.[12]

Diurnal regulation of excitability requires GTP

Constitutive G-protein activation of GIRK channels contributes to low intrinsic excitability of mature dentate GCs,[19] so we next tested whether diurnal differences in synaptic and intrinsic excitability relies on G-protein signaling by repeating recordings in the absence of Na-GTP (GTP^-) in the intracellular solution. In this condition, there was no difference in spike recruitment by perforant path stimulation during the Light and Dark phases (Figure 3A; contrast with 1C). Likewise, the number of APs generated by current injection was

equalized during the Light and Dark phases (Figure 3B), and the intrinsic properties were similar (RMP = −70.7 ± 0.2 versus −69.4 ± 0.7 mV; IR = 384 ± 18 versus 356 ± 21 MΩ; rheobase = 55.7 ± 3 versus 53.5 ± 3 pA) (Figure 3C). These results suggest that G-protein signaling is essential to generate diurnal rhythmicity, and its absence during the Light phase phenocopies the higher excitability observed during the Dark. Indeed, the lack of GTP in the pipette increases excitability of GCs during the Light phase,[19] whereas it had no effect on intrinsic excitability in GCs recorded during the Dark phase (Figure S3).

Diurnal regulation of G-protein gated K^+ and Na^+ conductances

To identify specific G-protein regulated channels that contribute to diurnal regulation of excitability, first we tested the prediction that there is a larger GIRK-mediated conductance during the Light phase, using a $GABA_B$ inverse agonist that suppresses constitutive GIRK channel activity (CGP55845, 10 μM; CGP).[19] As expected, CGP increased GC excitability, shifting the spike-current relationship to the left, depolarizing the RMP and increasing IR, thus reducing rheobase. However, CGP had no effect during the Dark phase (Figures 4A and 4B, red symbols). We also confirmed differential effects of CGP during Subjective Day and Night in DD mice (Figure S4). To test whether the differential effect of CGP is mediated via regulation of constitutive activity or downregulation of GIRK channels, we compared the actions of the GIRK-selective activator ML297 (10 μM). ML297 reduced the number of action potentials elicited by current injection, hyperpolarized the RMP, and decreased IR and excitability in both Light and Dark phases (Figures 4A and 4B, green symbols). In the presence of ML297, there were no differences in excitability between Light and Dark phases (Figure S4). This suggests that regulation of GIRK channel activity, rather than changes in the number of GIRK channels, contributes to the GTP-dependent diurnal rhythms in GC excitability.

The RMP and IR is set by the balance of leak Na^+ and K^+ currents, so we next evaluated a potential role of non-selective Na^+ leak channel (NALCN) activity using a selective blocker (L-703,606; 10 μM).[30] L-703,606 had no effect on GCs during the Light phase but hyperpolarized the RMP and increased the IR during the Dark phase (Figure 4C). These changes in passive properties during the Dark did not alter the number of action potentials elicited by current injections. To directly compare NALCN-mediated currents during the Light and Dark phases, we isolated the TTX-insensitive Na^+ conductance in the presence of synaptic and K^+ channel blockers and measured the shift in current sensitive to substitution of Na^+ ions by N-methyl-D-glutamine (NMDG). During the Light phase, there was no significant shift in membrane current by Na^+ substitution (3.5 ± 2.7 pA), consistent with minimal activity of NALCN in GCs in 2 mM extracellular Ca^{2+}[21]; however, during the Dark phase, NMDG caused a significant outward current (25.3 ± 2.5 pA) consistent with a tonic inward Na^+ current (Figure 4D, left). To confirm this current is mediated by NALCN, we repeated the experiment in 0.1 mM Ca^{2+} that potentiates NALCN channel activity.[31] In 0.1 mM Ca^{2+}, there was a small persistent Na^+ current during the Light phase (12.4 ± 2.4 pA) that was larger during the Dark phase (33.9 ± 3.5 pA; Figure 4D, middle). Finally, to test whether the lack of NALCN activity during the Light results from suppression by inhibitory G-protein signaling,[22] we measured the NMDG-sensitive current using an intracellular pipette solution containing GDPβS, a non-hydrolyzable GDP analogue

that prevents constitutive activation of GIRKs.[19] With GDPβS, a large NMDG-sensitive current developed gradually after achieving whole-cell configuration (Figure 4D). Together these results show that constitutive inhibitory G-protein signaling suppresses GC intrinsic excitability during the Light phase by both activating GIRKs and suppressing NALCN channels. Thus, diurnal rhythms of GC passive excitability are mediated by coordinated regulation of G-protein dependent K^+ and Na^+ conductances, reminiscent of the antiphase cycles that drive circadian control of membrane potential in master clock neurons.[23–25]

GTP-dependent diurnal regulation of spike bursts

GCs *in vivo* can fire brief high-frequency bursts of 2–4 action potentials important for recruitment of CA3 neurons via strongly facilitating mossy fiber synapses.[32] Although there were no significant differences in the properties of individual action potentials between the Light and Dark phases, including threshold (−39.3 ± 0.8 versus −40 ± 1.2 mV, p = 0.6), amplitude (83.5 ± 2 versus 88.1 ± 2.6 mV, p = 0.1), and width (0.71 ± 0.02 versus 0.75 ± 0.01 ms, p = 0.08), we observed a striking diurnal difference in the propensity for burst firing that was dependent upon intact G-protein signaling. During the Light phase, GCs exclusively exhibited a single action potential in response to rheobase current injection (Figure 5A) and perforant path stimulation (Figure 5B). However, GCs recorded in the Dark phase, or in the absence of intracellular GTP during the Light phase, often exhibited a burst of action potentials, defined by two or three action potentials at frequencies over 100 Hz. At rheobase, 31% and 36% of GCs showed bursting during the Dark phase or in the absence of GTP during the Light phase, respectively (Figure 5A). GCs also exhibited a greater propensity for burst firing in response to higher current injections during the Dark phase (Figure S5). Likewise, no GCs displayed action potential bursts in response to perforant path stimulation during the Light phase, yet 42% of GCs in the Dark phase exhibited bursting, and 18% of GCs in the Light phase exhibited bursting in the absence of GTP (Figure 5B). These results suggest that additional mechanisms beyond leak K^+ and Na^+ conductances likely contribute to diurnal regulation of excitability across the circadian cycle. One likely candidate is T-type Ca^{2+} channels that are implicated in GC bursting and are a target for $G_{I/o}$ signaling.[33,34]

Diurnal regulation of synaptic recruitment is disrupted by *Bmal1* cKO

Based on the daily cycle of core clock gene expression,[35] we wondered whether diurnal regulation of GC excitability relies on a cell-autonomous transcriptional oscillation. We used conditional *Bmal1* deletion to disrupt the molecular clock in dentate GCs while leaving SCN function intact.[36,37] We targeted GCs with a *Pomc-Cre* line that uses cryptic promoter regions to drive transient expression in developing GCs,[38,39] with minimal expression in other brain regions (Figure S6). To assess the efficiency of Cre targeting, we quantified co-localization between the Ai14 reporter (tdTomato; tdT) and the GC marker Prox1, finding 59% ± 2% of $Prox1^+$ GCs express tdT (900/1527 Prox1 cells from 7 cKO mice). Consistent with a restricted expression pattern, *Pomc-Cre*:*tdT*:$Bmal1^{lox/lox}$ mice (Bmal1 conditional KO; cKO) exhibited normal circadian locomotor rhythms in both light/dark (LD) and DD, indicating intact SCN function (Figure S6). Immunolabeling in cKO mice revealed loss of BMAL1 from the inner half of the granule cell layer where the majority of tdT^+ GCs are located (near the hilus), whereas tdT^- GCs located in the outer layer showed BMAL1

immunoreactivity similar to controls (Figure 6A). To quantify *Bmal1* deletion, we measured the intensity of BMAL1 immunoreactivity in linear regions of interest containing tdT^+ and tdT^- GCs from cKO and *Pomc-Cre*:*tdT*:*Bmal1*$^{wt/wt}$ (control) mice and found a negative correlation only in cKO mice (Figures 6B and 6C). Similarly, the intensity of BMAL1 immunoreactivity was lower in tdT^+ compared with tdT^- GCs in cKO mice, whereas there was no difference in control mice (Figure 6D).

The presence of Cre positive and negative GCs allowed us to determine the cell-autonomous effect of *Bmal1* deletion by recording from neighboring tdT^+ (*Bmal1* cKO) and tdT^- (*Bmal1* wild type [WT]) GCs within the same slices, and to directly compare synaptic recruitment by the same afferent fiber stimulation (Figure 6E). During the Light phase, *Bmal1* cKO GCs were more likely to spike in response to perforant path stimulation compared with neighboring WT GCs, revealing an increase in afferent recruitment at most stimulus intensities (Figure 6E, left). However, there was no difference in perforant path-evoked spiking during the Dark phase (Figure 6E, right). Interestingly, we also found a burst-like pattern in 28% of *Bmal1* cKO GCs during the Light phase (Figure 6F). These results suggest a cell-autonomous role of the molecular clock in reducing excitability of GCs specifically during the Light phase. The similar (high) excitability of tdT^+ and tdT^- GCs during the Dark reinforces the hypothesis that diurnal changes in GC excitability result from a molecular clock-dependent reduced excitability during the Light phase, rather than increased excitability during the Dark phase.

Diurnal regulation of intrinsic excitability is disrupted by *Bmal1* cKO

We next compared intrinsic excitability and its regulation by G-protein signaling in GCs from cKO mice. *Bmal1* WT GCs (tdT^-) exhibited the expected diurnal difference in intrinsic excitability shown in Figure 2, with a rightward shift in the spike-current relationship during the Light phase (Figure 7A, open symbols) and single action potentials (Figure 7B), along with a hyperpolarized RMP (−75.7 ± 0.4 versus −69.1 ± 1 mV) and increased rheobase (80 ± 3.3 versus 60.6 ± 4.2 pA) compared with the Dark phase (Figure 7C, light blue versus gray violin plots). However, neighboring *Bmal1* cKO GCs (tdT^+) failed to exhibit a diurnal difference in intrinsic excitability. Instead, during the Light phase, *Bmal1* cKO GCs phenocopied the Dark phase excitability (Figure 7A, solid symbols) and action potential burst pattern (Figure 7B), with the same depolarized RMP (−68.3 ± 0.8 versus −70 ± 0.8 mV) and rheobase (63.6 ± 4 versus 64.6 ± 4.4 pA) as during the Dark phase (Figure 7C, dark blue and black violin plots). Thus, *Bmal1* cKO GCs were more excitable than neighboring WT GCs only during the Light phase (Figures 7A–7C, light blue open symbols versus dark blue solid symbols). Importantly, the lack of diurnal regulation of synaptic recruitment and intrinsic excitability were dependent on the *Bmal1* floxed gene rather than Cre expression, as comparing intrinsic excitability and synaptic recruitment in tdT^+ and tdT^- GCs from control mice (*Pomc-Cre*:*tdT*:*Bmal1*$^{wt/wt}$) revealed no differences (Figure S7). Thus, deletion of *Bmal1* leads to a cell-autonomous deficit in diurnal regulation of GC excitability by preventing reduced excitability during the Light phase.

To confirm that the loss of diurnal regulation of excitability results from impairment of G-protein regulated K^+ and Na^+ channels, we assessed these currents in *Bmal1* cKO GCs

during the Light phase. In contrast to WT GCs that exhibit enhanced excitability in response to CGP, *Bmal1* cKO GCs showed no changes in the spike-current relationship (Figure 7D) and intrinsic properties (−70.6 ± 0.9 versus −71.9 ± 1.3 mV; 251 ± 20 versus 288 ± 10 MΩ; 64.1 ± 6.2 versus 61.5 ± 4.2 pA for RMP, IR, and rheobase, respectively) (Figure 7E). Furthermore, *Bmal1* cKO GCs exhibited a pronounced constitutive Na^+ current (21 ± 3.9 pA) that was absent in WT GCs (3.5 ± 2.7 pA, from Figure 4) (Figure 7F). Thus, *Bmal1* deletion removes constitutive G-protein regulation of K^+ and Na^+ conductances during the Light phase. Interestingly, while the spike-current relationship, RMP, rheobase, and constitutive K^+ and Na^+ current in *Bmal1* cKO GCs phenotypes the Dark phase, the IR did not (Figure 7C, middle). This suggests that the loss of the constitutive K^+ conductance (expected to increase IR) may be countered by an enhanced leak Na^+ conductance (expected to decrease IR), that together mask changes in IR despite the robust consequences on excitability.

Enhanced spatial memory in *Bmal1* cKO mice during the Light phase

Finally, we wondered whether conditional *Bmal1* deletion in GCs could alter a behavioral task that is specifically dependent upon GC excitability. Object location memory (OLM) is a simple test that evaluates the ability to discriminate and recollect when an object is moved from its original location. Discriminating small displacements relies on DG-CA3 pattern separation, exhibits diurnal variation with poor performance during the Light phase, and is sensitive to optogenetic modulation of GC excitability.[40–43] We first compared OLM performance of *Bmal1* cKO and control mice during the Light phase. On the training day, cKO and control mice spent a similar amount of time exploring two objects in an open field. When reintroduced into the field 24 h later, cKO mice spent more time exploring the object placed in the new location compared with the object in the same location, and the discrimination ratio revealed that *Bmal1* cKO mice had a greater preference for the moved object compared with controls (Figure S8A). We tested a separate cohort of mice on the same OLM task during the Dark phase. In this case, on the test day both control and cKO mice spent more time exploring the moved object compared with the object in the same location and there was no difference in the discrimination ratio between genotypes (Figure S8B). These results show that *Bmal1* cKO mice have enhanced OLM performance only during the Light phase, mirroring changes in GC excitability that were also evident during the Light.

DISCUSSION

There is limited understanding of circadian regulation of membrane physiology outside of the SCN (reviewed in Paul et al.[2]). Early work – showed that DG population spikes in rats and squirrel monkeys are enhanced during active periods[12]; however, the cellular mechanisms contributing to differential excitability and whether these oscillations are under cell-intrinsic control were not clear. In contrast, it is well known that SCN neurons under the supervision of clock transcriptional components exhibit circadian oscillations in membrane intrinsic properties that are regulated by various mechanisms including channel trafficking, kinase activity, and auxiliary subunit expression.[23,24,27,44]

Here we demonstrate that GCs exhibit reduced excitability during the Light phase in a manner independent of $GABA_A$ receptor-mediated inhibition. Measures of intrinsic excitability including RMP, IR, and rheobase oscillate with a period of approximately 24 h controlled by a GTP-dependent mechanism. Constitutive antiphase K^+ and Na^+ leak conductances, both regulated by inhibitory G-protein signaling, drive rhythmic depolarization and hyperpolarization when *Bmal1* expression is intact. Hence, chronodisruption by conditional deletion of *Bmal1* enhanced GC excitability only during the Light phase. These results show that cell-autonomous transcriptional regulation requiring *Bmal1* reduces GC excitability during the Light phase via disruption of G-protein signaling, illustrating a novel mechanism coupling membrane excitability by antiphase K^+ and Na^+ conductances to the molecular clock.

The efficiency of synaptic recruitment depends on interactions of synaptic conductances with the passive and active properties of the membrane. We found reduced cortical recruitment of GCs during the Light phase. Low intrinsic excitability contributes to differential recruitment by perforant path synaptic stimulation because (1) differences in spiking were readily apparent using current injections to isolate membrane properties; (2) differences remained in the presence of GBZ but were (3) absent when we excluded GTP from the pipette recording solution; and (4) our conditional deletion model allows us to compare synaptic recruitment of neighboring GCs with intrinsic excitability suppressed or intact by *Bmal1* deletion. In addition to our focus on intrinsic excitability, it is also likely that multiple cortical-hippocampal network components exhibit diurnal regulation excitability including the network of GABAergic interneurons and EC synaptic activity.[2,7,45]

- $GABA_B$ receptor activation opens GIRK channels in mature GCs, whereas it suppresses Ca^{2+} currents in young adult-born GCs that lack functional GIRK coupling.[19,46] Here we show constitutive $GABA_B$/GIRK activity in mature GCs also changes over the light cycle. Most basal activity of GIRK is Gβγ-dependent, thus changes in Gβγ availability likely underlie the constitutive GIRK conductance.[47] This idea is also supported by our observation of larger constitutive Na^+ currents during the Dark phase. The Na^+ leak conductance exhibits hallmarks of NALCN since it is potentiated by low extracellular Ca^{2+} and inhibited by Gβγ, and a selective NALCN blocker hyperpolarizes GCs during the Dark.[22,31] Our results are consistent with the recent finding that NALCN normally has a minimal effect on GC excitability (during the Light phase), but it can be potentiated by posttranslational modification.[21] Together our results suggest that the presence of free Gβγ during the Light phase both constitutively activates GIRKs while inhibiting NALCN, but other channels could also be affected, including those that contribute to burst firing.[33] Diurnal variation in free Gβγ could result from several mechanisms. Regulators of G-protein signaling (RGS) bind to activated Gα subunits to accelerate GTPase activity thereby reducing free Gβγ,[48] and both activators of G-protein signaling (AGS) and G-protein receptor kinases (GRK) linked to arrestins can regulate Gβγ availability.[49] Components of the GTP signaling system are circadian-regulated genes in diverse organisms, suggesting that G-protein-regulated membrane excitability may also be a conserved mechanism in other populations of neurons across different organisms.[4,24,25,50–52]

We linked G-protein regulation of K^+ and Na^+ channels to the circadian molecular clock using conditional deletion of *Bmal1*,a core clock gene. *Bmal1* deletion caused GCs during the Light phase to phenocopy the higher excitability of the Dark phase, with no apparent differences during the Dark phase. We used a *Pomc-Cre* line that primarily targets *Bmal1* deletion to early postmitotic GCs in the DG,[38,39] and our experimental design argues against a major involvement of other cell populations in the effects on GC excitability. First, cKO mice exhibit normal circadian rhythms in both LD and DD conditions, indicating intact SCN function. Second, during the Light phase, neighboring *Bmal1* cKO and WT GCs differed in intrinsic properties and afferent recruitment, excluding the possibility that a diffusible substance or other network component mediates the difference in excitability. Third, we did not detect differences between tdT^- GCs in cKO and unlabeled GCs in WT mice, or between tdT^+ and tdT^- GCs in *Pomc-Cre*:*Bmal1*$^{+/+}$: *Ai14* controls, ruling out non-cell-autonomous effects of *Bmal1* deletion and non-specific effects of transient Cre expression, respectively. Because discordance between recombination of multiple *loxP* alleles predicts some tdT^+ GCs in *Bmal1* cKO mice have intact *Bmal1* (see Figure 6B),[53] our results comparing tdT^+ and tdT^- GCs in cKO mice likely underestimates the full effect of *Bmal1* deletion on individual GC excitability.

Limitations of the study

While the effect of *Bmal1* deletion on GC intrinsic excitability is likely due to cell-autonomous regulation by G-protein signaling, additional cell populations or mechanisms can contribute to the differences we found in spatial discrimination. Enhanced GC excitability in cKO mice during the Light correlated with improved performance on an OLM task that relies on DG-CA3 circuit pattern separation.[42] This result is consistent with reliance of this task on both DG excitability and time of day, with better discrimination during the Dark phase.[40,41,43] In contrast, deletion of *Bmal1* using *CamKII-Cre* selectively impaired spatial discrimination during the Dark,[43] possibly due to differences between cell-type-specific targeting, and/or differential reliance on memory consolidation/retrieval processes that also depend on the intact molecular clock in forebrain neurons.[43,54,55] Future studies will be required to determine the molecular signaling pathway mediating G-protein regulation of GC intrinsic excitability and its contribution to circadian-regulated behaviors.

In conclusion, our results provide new insight into the role of the local molecular clock in the control of neuronal excitability. In addition to coordinated regulation of resting K^+ and Na^+ membrane conductances, changes in the pattern of GC spiking suggests voltage-activated channels are controlled by diurnal regulation of G-protein signaling. Short, high-frequency bursts of GC spikes have been reported in active GCs *in vivo*, and there is increased propensity for this form of bursting in GCs from epileptic tissue.[32,56,57] Considering the established role of the DG as the hippocampal gate for seizure propagation and recent evidence that disruption of circadian transcriptional loops modify seizure thresholds,[8,9] our findings present a promising inroad to address a chronotherapeutic approach in the management of temporal lobe epilepsy.[58]

STAR★METHODS

RESOURCE AVAILABILITY

Lead contact—Further information and request for resources and reagents should be directed to and will be fulfilled by the lead contact, Linda Overstreet-Wadiche (lwadiche@uab.edu).

Materials availability—This study did not generate new unique plasmids, mouse lines or reagents.

Data and code availability

- All data reported in this paper will be shared by the lead contact upon request.
- This paper does not report original code.
- Any additional information required to reanalyze the data reported in this paper is available from the lead contact upon request.

EXPERIMENTAL MODEL AND SUBJECT DETAILS

Animals—We used two-to five-month-old male and female mice from colonies of WT C57BL/6J (Jackson #000664), nNOS-CreERt2 (Jackson #014541); PV-Cre (Jackson #017320); Ai14 (Jackson #007914) and Ai32 (Jackson #024109) mice, all maintained on a C57BL/6J background. Diurnal differences in GC intrinsic properties were detected in male and female mice from all lines, so data were pooled. To conditionally delete *Bmal1* from dentate GCs, first we crossed *Pomc-Cre* mice (Jackson #:010714; on a C57Bl/6J background) with $Bmal1^{lox}$ mice (Jackson # 007668) to generate $Pomc\text{-}Cre^{+}$:$Bmal1^{lox/lox}$ mice. These were subsequently crossed with $Bmal1^{lox/lox}$; Ai14 reporter mice (Jackson #007914) to obtain $Pomc\text{-}Cre^{+}$:$Bmal1^{lox/lox}$:*Ai14* (*Bmal1* cKO and Cre^{-} control) mice used in experiments (Figure S6). As additional controls, we also crossed *Pomc-Cre* mice with Ai14 reporter mice ($Pomc\text{-}Cre^{+}$:$Bmal1^{+/+}$:*Ai14*). Genotypes were identified by PCR using following primer sets: for Cre: oIMR 1084 (GCG GTC TGG CAG TAA AAA CTA TC); oIMR 1085 (GTG AAA CAG CAT TGC TGT CAC TT); oIMR 7338 (CTA GGC CAC AGA ATT GAA AGA TCT) and oIMR 7339 (GTA GGT GGA AAT TCT AGC ATc ATC C). For *Bmal1*: oIMR 7525 (ACT GGA AGT AAC TTT ATC AAA CTG) and oIMR 7526 (CTG ACC AAC TTG CTA ACA ATT A). Mice were housed in standard cages with ad libitum access to food and water and maintained in 12:12 light/dark (LD) cycle, except animals used for monitoring circadian wheel-running activity. These mice were housed individually in cages equipped with running wheels (Coulbourn Instruments, Whitehall, PA, USA) in LD for at least 15 days before being released into DD. During constant darkness, circadian time (CT) 12 equals activity onset and the beginning of subjective night. All procedures were approved by the University of Alabama at Birmingham Institutional Animal Care and use Committee (IACUC) in accordance with the US National Institute of Health Guide for the Care and Use of Laboratory Animals.

METHODS DETAILS

Slice preparation—Slices were prepared from mice sacrificed at ZT 5.5 or ZT 11.5 for Light and Dark phase recordings, respectively. Mice were anesthetized with 4% Isoflurane (Fluriso™, USP; Vet One), and 2,2,2-tribromoethanol (Avertin; Sigma-Aldrich) and perfused intracardially with ice-cold modified artificial cerebrospinal fluid (ACSF) cutting solution containing the following (in mM): 110 choline chloride, 7 $MgCl_2$, 2.5 KCl, 1.25 Na_2PO_4, 0.5 $CaCl_2$, 1.3 Na-ascorbate, 3 Na-pyruvate, 25 D-glucose and 25 $NaHCO_3$, bubbled with 5% CO_2/95% O_2. The brain was quickly removed, and 300 μm horizontal slices were prepared using a vibratome (VT1200S, Leica instruments). Slices were incubated at 37°C for ~30 min, then transferred to room temperature in recording solution containing the following (in mM): 125 NaCl, 2.5 KCl, 1.25 Na_2PO_4, 1 $MgCl_2$, 2 $CaCl_2$, 25 D-glucose and 25 $NaHCO_3$ bubbled with 5% CO_2/95% O_2. Slices were also prepared at ZT 0 and ZT 18 for Figure 2. ZT 18 and DD mice were handled under dim light and perfused with the eyes covered to avoid light interference. Recordings were started 2 h after slice preparation during a 3-h window (ZT 8–11, Light phase or CT 8–11 Subjective Day; ZT 14–17, Dark phase or CT 14–17, Subjective Night), except for Figure 2, where additional cells were recorded before and after the recording window to cover the entire 24 h cycle.

Electrophysiology—Visually identified granule cells in the suprapyramidal and infrapyramidal blade were patched in the whole-cell configuration. GCs expressing tdTomato were visualized using epifluorescence illumination and a Texas Red filter set. GCs in the middle of the granule cell layer were targeted for recording to avoid immature adult-born GCs and semilunar GCs. GCs with intrinsic properties consist with immature or semilunar GCs were discarded. Fire-polished borosilicate glass electrodes (BF150–86-10, Sutter Instrument) with resistance of 2–4 MΩ when filled with intracellular solution were mounted on the headstage (CV-7B) of a Multiclamp 700A amplifier (Molecular Devices). Pipettes for current clamp recordings were filled with the following (in mM): 135 K-gluconate, 3 KCl, 2 $MgCl_2$, 10 HEPES, 0.1 EGTA, 10 phosphocreatine, 2 Mg-ATP and 0.5 Na-GTP (excluded in GTP^- experiments), pH 7.3 and 310 mOsm. After cancellation of pipette capacitive transients, intrinsic properties were measured in current-clamp mode (no injected current) after using bridge balance to compensate series resistance (<25mΩ). Voltages were not corrected for junction potentials, calculated to be 13.6 mV. All recordings were made at 30°C and experiments were discarded if substantial changes bridge balance were detected. Currents were sampled at 10kHz and filtered at 2kHz (Digidata 1440A; Molecular Devices) using PClamp 10 software (Molecular Devices). Stimulation of the perforant path (100 ms; 20–100 in increments of 10 mA and 200 mA, 3–5 sweeps per intensity at 10 s intervals) was achieved using a patch pipette (1–2 MΩ) filled with recording solution and controlled by a constant-current isolated stimulator (Digitimer Ltd). To avoid directly stimulating local GABAergic interneurons, electrodes were placed at a distance from the recorded cells, adjacent to the hippocampal fissure between the suprapyramidal blade and apex of the GCL (defined as the midpoint between the suprapyramidal and infrapyramidal blades) to stimulate both lateral and medial perforant path. Sequential ‘‘paired’’ recordings of *Bmal1* cKO and neighboring *Bmal1* WT GCs were made without changing the stimulation parameters.

Current steps (500 ms) were injected in increments of 10 pA from −10 to 150 pA, and the number of spikes were quantified for each step to generate an input-output curve of neuronal excitability. Rheobase was defined by the minimum current needed to elicit an action potential. Intrinsic passive properties including RMP, IR and TC were calculated using the average of 50 sweeps from a −10 pA current injection.

For voltage clamp experiments, pipettes were filled with (in mM): 122 $CsMeSO_3$, 1.8 $MgCl_2$, 9 HEPES, 0.45 EGTA, 14 phosphocreatine, 0.09 $CaCl_2$, 4 Mg-ATP and 0.5 Na-GTP. Recording solution was composed of (in mM): 125 NaCl, 2.5 KCl, 1$MgCl_2$, 1.25 Na_2PO_4, 2 $CaCl_2$, 25 $NaHCO_3$ and 25 D-glucose (bubbled with 95% O_2/5% CO_2). For Na^+ substitution, 125 NaCl was replaced with 125 N-Methyl-D-glutamine (NMDG).[22] GCs were held at −70 mV and recordings were performed in presence of external NBQX (10 μM), R-CPP (50 μM), PTX (50 mμM), TTX (1 μM), $BaCl_2$ (100 μM), apamin (300 nM) and $CsCl_2$ (3 mM).

Data were analyzed with Clampfit (Molecular Devices) and Axograph X (Axograph Scientific). Drugs and chemicals were obtained from Ascent Scientific, Sigma-Aldrich or Tocris Bioscience.

Immunohistochemistry—Mice were intracardially perfused with 0.1 M PBS followed by chilled 4% paraformaldehyde (PFA) before brains were removed and post-fixed overnight in 4% PFA. Fifty micrometer free-floating horizontal sections through the entire brain (Vibratome 3000) were stored at −20°C in antifreeze solution (30% ethylene glycol, 20% glycerol in PBS). For Prox-1 immunostaining, slices were washed in PBS and permeabilized and blocked with 0.4% Triton X-100 and 10% normal donkey serum, 3% BSA and 1% glycine for 90 min at room temperature. Then, sections were incubated overnight at 4°C with anti-Prox1 antibody (1:500; AF2727, goat anti h-Prox1; R&D Systems), washed and incubated with donkey anti-goat Alexa Fluor 647 (1:500; Invitrogen; 3 h at room temperature). For BMAL1 immunostaining, slices were washed in PBS and permeabilized and blocked with 0.3% Triton X-100 and 5% BSA for 1 h at room temperature. Then sections were incubated overnight at 4°C with anti-BMAL1 antibody (1:2000; NB100–2288, rabbit anti-BMAL1; Novus Biologicals), washed and incubated with goat anti-rabbit Alexa Fluor 488 (1:1000; Invitrogen; 1 h at room temperature). Sections were mounted using Vectashield or Prolong Gold mounting medium (Invitrogen) and imaged using an Olympus FV1200 Confocal Microscope with a 20× or 40× water-immersion objective. Images from *Bmal1* cKO and controls were acquired with the same microscope settings and analyzed without adjustment (ImageJ software) using a linear region of interest (ROI) drawn across the soma of 3–5 neighboring tdT^+ and tdT^- cells. ROIs were selected solely by tdT expression from 18 sections from 3 control mice and 16 sections from 6 cKO mice. The Plot Profile option was used to obtain an arbitrary gray value along each point of the ROI in both the red and green channels, and the R value for the correlation at each point was found using Prism (GraphPad Software).

Behavior—Behavior analyses were performed in dim lighting conditions during the Light window (ZT 8–11) or Dark window (ZT 14–17). Researchers conducting and analyzing behavior assays were blind to genotype. Male mice were habituated to researchers for

7 consecutive days prior to testing object location memory (OLM).[59] For OLM testing, mice were habituated to a white plexiglass testing chamber (39 × 19 × 21 cm) with fresh bedding material for 2 consecutive days. On training day, two similar plastic bath toy objects were placed on one side of the box and mice were allowed to freely explore for 10 min. Twenty-four hours later, mice were returned to the box for 5 min where 1 object was displaced to the center of the box (see Figure S8). Mouse behavior was recorded (TopScan, CleverSys 2.0, Reston, VA, USA) and videos were manually scored by a different blinded investigator. Interaction was judged to occur if mice were sniffing within 2 cm of a given object. Mice had to explore each object for at least 5 s during the training phase and 15 s during testing to be included; no mice failed minimum interaction requirements. During training, mice were excluded if they displayed object/side preference greater than 20%; 1 mouse required exclusion. Percent discrimination was calculated as % of time spent with the moved object–time spent with the non-moved object/total time.

For assessment of circadian locomotor rhythms, mice were individually housed with running wheels initially in a 12:12 light-dark cycle (LD) for at least 15 days before being released into constant dark (DD). Wheel-running activity was recorded and analyzed using ClockLab software (Actimetrics, Wilmette, IL). Behavior was analyzed across 10 days of activity. Activity levels were calculated using the batch analysis function in ClockLab software.

QUANTIFICATION AND STATISTICAL ANALYSIS

Data is presented as median and quartile lines in violin plots and as mean ± s.e.m. in dot plots and histograms. To compare number of spikes elicited by current steps, areas under the curve were measured as suggested by statistic guide of GraphPad followed by a t test or one-way ANOVA. Group comparison used chi-squared (χ^2), two-sample paired or unpaired t test, multiple unpaired t tests comparison by Holm-Sidak method or ANOVA with datasets that satisfied normality criteria, while non-normal datasets were analyzed with Mann-Whitney test (Prism; GraphPad Software). For actograms, the free-running period and amplitude were determined by chi-squared (χ^2) periodogram analysis. Data were analyzed using a one-way ANOVA with LSD post-hoc tests. Rhythmic comparison of intrinsic properties was calculated using Cosinor analysis using SPSS (version 25) and the following equation.

$$f(t) = \text{Mesor} + A * \text{Cos}[(2 \quad pt/T) + \text{Acrophase}]$$

where

Mesor (acronym for middle estimating statistic of rhythm) = the mean of the oscillation

A = the amplitude (peak-to-trough difference) T = the period (24 h)

Acrophase = the timing of the cosine maximum t = a time point

R^2 is the resulting statistic that measures the percent variance accounted for by the 24 h approximating waveform.

Supplementary Material

Refer to Web version on PubMed Central for supplementary material.

ACKNOWLEDGMENTS

This work was supported by an American Epilepsy Society fellowship (J.C.G.); NIH R01NS082413 (K.L.G.), NIH R01NS113948 (J.I.W.), and R01NS064025 and R01NS105438 (L.O.-W.). We thank all members of the Wadiche labs for helpful comments throughout this project and Mary Seelig for technical assistance.

REFERENCES

1. Hastings MH, Maywood ES, and Brancaccio M (2018). Generation of circadian rhythms in the suprachiasmatic nucleus. Nat. Rev. Neurosci 19, 453–469. 10.1038/s41583-018-0026-z. [PubMed: 29934559]
2. Paul JR, Davis JA, Goode LK, Becker BK, Fusilier A, Meador-Woodruff A, and Gamble KL (2020). Circadian regulation of membrane physiology in neural oscillators throughout the brain. Eur. J. Neurosci 51, 109–138. 10.1111/ejn.14343. [PubMed: 30633846]
3. Brüning F, Noya SB, Bange T, Koutsouli S, Rudolph JD, Tyagarajan SK, Cox J, Mann M, Brown SA, and Robles MS (2019). Sleep-wake cycles drive daily dynamics of synaptic phosphorylation. Science 366, eaav3617. 10.1126/science.aav3617. [PubMed: 31601740]
4. Noya SB, Colameo D, Brüning F, Spinnler A, Mircsof D, Opitz L, Mann M, Tyagarajan SK, Robles MS, and Brown SA (2019). The forebrain synaptic transcriptome is organized by clocks but its proteome is driven by sleep. Science 366, eaav2642. 10.1126/science.aav2642. [PubMed: 31601739]
5. Bridi MCD, Zong FJ, Min X, Luo N, Tran T, Qiu J, Severin D, Zhang XT, Wang G, Zhu ZJ, et al. (2020). Daily oscillation of the excitation-inhibition balance in visual cortical circuits. Neuron 105, 621–629.e4. 10.1016/j.neuron.2019.11.011. [PubMed: 31831331]
6. Liu ZW, Faraguna U, Cirelli C, Tononi G, and Gao XB (2010). Direct evidence for wake-related increases and sleep-related decreases in synaptic strength in rodent cortex. J. Neurosci 30, 8671–8675. 10.1523/JNEUROSCI.1409-10.2010. [PubMed: 20573912]
7. Vyazovskiy VV, Cirelli C, Pfister-Genskow M, Faraguna U, and Tononi G (2008). Molecular and electrophysiological evidence for net synaptic potentiation in wake and depression in sleep. Nat. Neurosci 11, 200–208. 10.1038/nn2035. [PubMed: 18204445]
8. Wu H, Liu Y, Liu L, Meng Q, Du C, Li K, Dong S, Zhang Y, Li H, and Zhang H (2021). Decreased expression of the clock gene Bmal1 is involved in the pathogenesis of temporal lobe epilepsy. Mol. Brain 14, 113. 10.1186/s13041-021-00824-4. [PubMed: 34261484]
9. Zhang T, Yu F, Xu H, Chen M, Chen X, Guo L, Zhou C, Xu Y, Wang F, Yu J, and Wu B (2021). Dysregulation of REV-ERBalpha impairs GABAergic function and promotes epileptic seizures in preclinical models. Nat. Commun 12, 1216. 10.1038/s41467-021-21477-w. [PubMed: 33619249]
10. Debski KJ, Ceglia N, Ghestem A, Ivanov AI, Brancati GE, Bröer S, Bot AM, Müller JA, Schoch S, Becker A, et al. (2020). The circadian dynamics of the hippocampal transcriptome and proteome is altered in experimental temporal lobe epilepsy. Sci. Adv 6, eaat5979. 10.1126/sciadv.aat5979. [PubMed: 33036982]
11. Snider KH, Sullivan KA, and Obrietan K (2018). Circadian regulation of hippocampal-dependent memory: circuits, synapses, and molecular mechanisms. Neural Plast 2018, 7292540. 10.1155/2018/7292540. [PubMed: 29593785]
12. Barnes CA, McNaughton BL, Goddard GV, Douglas RM, and Adamec R (1977). Circadian rhythm of synaptic excitability in rat and monkey central nervous system. Science 197, 91–92. 10.1126/science.194313. [PubMed: 194313]
13. Dieni CV, Nietz AK, Panichi R, Wadiche JI, and Overstreet-Wadiche L (2013). Distinct determinants of sparse activation during granule cell maturation. J. Neurosci 33, 19131–19142. 10.1523/JNEUROSCI.2289-13.2013. [PubMed: 24305810]

14. Coulter DA, and Carlson GC (2007). Functional regulation of the dentate gyrus by GABA-mediated inhibition. Prog. Brain Res 163, 235–243. 10.1016/S0079-6123(07)63014-3. [PubMed: 17765722]
15. Erwin SR, Sun W, Copeland M, Lindo S, Spruston N, and Cembrowski MS (2020). A sparse, spatially biased subtype of mature granule cell dominates recruitment in hippocampal-associated behaviors. Cell Rep 31, 107551. 10.1016/j.celrep.2020.107551. [PubMed: 32348756]
16. Zhang X, Schlögl A, and Jonas P (2020). Selective routing of spatial information flow from input to output in hippocampal granule cells. Neuron 107, 1212–1225.e7. 10.1016/j.neuron.2020.07.006. [PubMed: 32763145]
17. Diamantaki M, Frey M, Berens P, Preston-Ferrer P, and Burgalossi A (2016). Sparse activity of identified dentate granule cells during spatial exploration. Elife 5, e20252. 10.7554/eLife.20252. [PubMed: 27692065]
18. Kim KR, Lee SY, Yoon SH, Kim Y, Jeong HJ, Lee S, Suh YH, Kang JS, Cho H, Lee SH, et al. (2020). Kv4.1, a key ion channel for low frequency firing of dentate granule cells, is crucial for pattern separation. J. Neurosci 40, 2200–2214. 10.1523/JNEUROSCI.1541-19.2020. [PubMed: 32047055]
19. Gonzalez JC, Epps SA, Markwardt SJ, Wadiche JI, and Overstreet-Wadiche L (2018). Constitutive and synaptic activation of GIRK channels differentiates mature and newborn dentate granule cells. J. Neurosci 38, 6513–6526. 10.1523/JNEUROSCI.0674-18.2018. [PubMed: 29915136]
20. Yarishkin O, Lee DY, Kim E, Cho CH, Choi JH, Lee CJ, Hwang EM, and Park JY (2014). TWIK-1 contributes to the intrinsic excitability of dentate granule cells in mouse hippocampus. Mol. Brain 7, 80. 10.1186/s13041-014-0080-z. [PubMed: 25406588]
21. Lee SY, Vuong TA, Wen X, Jeong HJ, So HK, Kwon I, Kang JS, and Cho H (2019). Methylation determines the extracellular calcium sensitivity of the leak channel NALCN in hippocampal dentate granule cells. Exp. Mol. Med 51, 1–14. 10.1038/s12276-019-0325-0.
22. Philippart F, and Khaliq ZM (2018). Gi/o protein-coupled receptors in dopamine neurons inhibit the sodium leak channel NALCN. Elife 7, e40984. 10.7554/eLife.40984. [PubMed: 30556810]
23. Paul JR, DeWoskin D, McMeekin LJ, Cowell RM, Forger DB, and Gamble KL (2016). Regulation of persistent sodium currents by glycogen synthase kinase 3 encodes daily rhythms of neuronal excitability. Nat. Commun 7, 13470. 10.1038/ncomms13470. [PubMed: 27841351]
24. Flourakis M, Kula-Eversole E, Hutchison AL, Han TH, Aranda K, Moose DL, White KP, Dinner AR, Lear BC, Ren D, et al. (2015). A conserved bicycle model for circadian clock control of membrane excitability. Cell 162, 836–848. 10.1016/j.cell.2015.07.036. [PubMed: 26276633]
25. Doi M, Ishida A, Miyake A, Sato M, Komatsu R, Yamazaki F, Kimura I, Tsuchiya S, Kori H, Seo K, et al. (2011). Circadian regulation of intracellular G-protein signalling mediates intercellular synchrony and rhythmicity in the suprachiasmatic nucleus. Nat. Commun 2, 327. 10.1038/ncomms1316. [PubMed: 21610730]
26. Cao G, and Nitabach MN (2008). Circadian control of membrane excitability in Drosophila melanogaster lateral ventral clock neurons. J. Neurosci 28, 6493–6501. 10.1523/JNEUROSCI.1503-08.2008. [PubMed: 18562620]
27. Kuhlman SJ, and McMahon DG (2004). Rhythmic regulation of membrane potential and potassium current persists in SCN neurons in the absence of environmental input. Eur. J. Neurosci 20, 1113–1117. 10.1111/j.1460-9568.2004.03555.x. [PubMed: 15305881]
28. Yu EP, Dengler CG, Frausto SF, Putt ME, Yue C, Takano H, and Coulter DA (2013). Protracted postnatal development of sparse, specific dentate granule cell activation in the mouse hippocampus. J. Neurosci 33, 2947–2960. 10.1523/JNEUROSCI.1868-12.2013. [PubMed: 23407953]
29. LeGates TA, Fernandez DC, and Hattar S (2014). Light as a central modulator of circadian rhythms, sleep and affect. Nat. Rev. Neurosci 15, 443–454. 10.1038/nrn3743. [PubMed: 24917305]
30. Hahn S, Kim SW, Um KB, Kim HJ, and Park MK (2020). N-benzhydryl quinuclidine compounds are a potent and Src kinase-independent inhibitor of NALCN channels. Br. J. Pharmacol 177, 3795–3810. 10.1111/bph.15104. [PubMed: 32436268]

31. Lu B, Zhang Q, Wang H, Wang Y, Nakayama M, and Ren D (2010). Extracellular calcium controls background current and neuronal excitability via an UNC79-UNC80-NALCN cation channel complex. Neuron 68, 488–499. 10.1016/j.neuron.2010.09.014. [PubMed: 21040849]
32. Pernía-Andrade AJ, and Jonas P (2014). Theta-gamma-modulated synaptic currents in hippocampal granule cells in vivo define a mechanism for network oscillations. Neuron 81, 140–152. 10.1016/j.neuron.2013.09.046. [PubMed: 24333053]
33. Dumenieu M, Senkov O, Mironov A, Bourinet E, Kreutz MR, Dityatev A, Heine M, Bikbaev A, and Lopez-Rojas J (2018). The low-threshold calcium channel Cav3.2 mediates burst firing of mature dentate granule cells. Cereb. Cortex 28, 2594–2609. 10.1093/cercor/bhy084. [PubMed: 29790938]
34. Scott RH, Wootton JF, and Dolphin AC (1990). Modulation of neuronal T-type calcium channel currents by photoactivation of intracellular guanosine 5'-O(3-thio) triphosphate. Neuroscience 38, 285–294. 10.1016/0306-4522(90)90028-3. [PubMed: 2175853]
35. Jilg A, Lesny S, Peruzki N, Schwegler H, Selbach O, Dehghani F, and Stehle JH (2010). Temporal dynamics of mouse hippocampal clock gene expression support memory processing. Hippocampus 20, 377–388. 10.1002/hipo.20637. [PubMed: 19437502]
36. Storch KF, Paz C, Signorovitch J, Raviola E, Pawlyk B, Li T, and Weitz CJ (2007). Physiological importance of a circadian clock outside the suprachiasmatic nucleus. Cold Spring Harb. Symp. Quant. Biol 72, 307–318. 10.1101/sqb.2007.72.053. [PubMed: 18419288]
37. Bunger MK, Wilsbacher LD, Moran SM, Clendenin C, Radcliffe LA, Hogenesch JB, Simon MC, Takahashi JS, and Bradfield CA (2000). Mop3 is an essential component of the master circadian pacemaker in mammals. Cell 103, 1009–1017. 10.1016/s0092-8674(00)00205-1. [PubMed: 11163178]
38. Overstreet LS, Hentges ST, Bumaschny VF, de Souza FSJ, Smart JL, Santangelo AM, Low MJ, Westbrook GL, and Rubinstein M (2004). A transgenic marker for newly born granule cells in dentate gyrus. J. Neurosci 24, 3251–3259. 10.1523/JNEUROSCI.5173-03.2004. [PubMed: 15056704]
39. McHugh TJ, Jones MW, Quinn JJ, Balthasar N, Coppari R, Elmquist JK, Lowell BB, Fanselow MS, Wilson MA, and Tonegawa S (2007). Dentate gyrus NMDA receptors mediate rapid pattern separation in the hippocampal network. Science 317, 94–99. 10.1126/science.1140263. [PubMed: 17556551]
40. Goode LK, Fusilier AR, Remiszewski N, Reeves JM, Abiraman K, Defenderfer M, Paul JR, McMahon LL, and Gamble KL (2022). Examination of diurnal variation and sex differences in hippocampal neurophysiology and spatial memory. eNeuro 9, ENEURO.0124–22.2022. 10.1523/ENEURO.0124-22.2022.
41. Pofahl M, Nikbakht N, Haubrich AN, Nguyen T, Masala N, Distler F, Braganza O, Macke JH, Ewell LA, Golcuk K, and Beck H (2021). Synchronous activity patterns in the dentate gyrus during immobility. Elife 10, e65786. 10.7554/eLife.65786. [PubMed: 33709911]
42. van Goethem NP, van Hagen BTJ, and Prickaerts J (2018). Assessing spatial pattern separation in rodents using the object pattern separation task. Nat. Protoc 13, 1763–1792. 10.1038/s41596-018-0013-x. [PubMed: 30038346]
43. Snider KH, Dziema H, Aten S, Loeser J, Norona FE, Hoyt K, and Obrietan K (2016). Modulation of learning and memory by the targeted deletion of the circadian clock gene Bmal1 in forebrain circuits. Behav. Brain Res 308, 222–235. 10.1016/j.bbr.2016.04.027. [PubMed: 27091299]
44. Whitt JP, Montgomery JR, and Meredith AL (2016). BK channel inactivation gates daytime excitability in the circadian clock. Nat. Commun 7, 10837. 10.1038/ncomms10837. [PubMed: 26940770]
45. Cirelli C (2017). Sleep, synaptic homeostasis and neuronal firing rates. Curr. Opin. Neurobiol 44, 72–79. 10.1016/j.conb.2017.03.016. [PubMed: 28399462]
46. Gao Y, Shen M, Gonzalez JC, Dong Q, Kannan S, Hoang JT, Eisinger BE, Pandey J, Javadi S, Chang Q, et al. (2020). RGS6 mediates effects of voluntary running on adult hippocampal neurogenesis. Cell Rep 32, 107997. 10.1016/j.celrep.2020.107997. [PubMed: 32755589]

47. Rishal I, Porozov Y, Yakubovich D, Varon D, and Dascal N (2005). Gbetagamma-dependent and Gbetagamma-independent basal activity of G protein-activated K+ channels. J. Biol. Chem 280, 16685–16694. 10.1074/jbc.M412196200. [PubMed: 15728579]
48. Lin C, Koval A, Tishchenko S, Gabdulkhakov A, Tin U, Solis GP, and Katanaev VL (2014). Double suppression of the Galpha protein activity by RGS proteins. Mol. Cell 53, 663–671. 10.1016/j.molcel.2014.01.014. [PubMed: 24560274]
49. Gurevich VV, and Gurevich EV (2019). GPCR signaling regulation: the role of GRKs and arrestins. Front. Pharmacol 10, 125. 10.3389/fphar.2019.00125. [PubMed: 30837883]
50. Nakagawa S, Nguyen Pham KT, Shao X, and Doi M (2020). Time-restricted G-protein signaling pathways via GPR176, Gz, and RGS16 set the pace of the master circadian clock in the suprachiasmatic nucleus. Int. J. Mol. Sci 21, 5055. 10.3390/ijms21145055. [PubMed: 32709014]
51. Olmedo M, O'Neill JS, Edgar RS, Valekunja UK, Reddy AB, and Merrow M (2012). Circadian regulation of olfaction and an evolutionarily conserved, nontranscriptional marker in Caenorhabditis elegans. Proc. Natl. Acad. Sci. USA 109, 20479–20484. 10.1073/pnas.1211705109. [PubMed: 23185015]
52. Takahashi H, Umeda N, Tsutsumi Y, Fukumura R, Ohkaze H, Sujino M, van der Horst G, Yasui A, Inouye SIT, Fujimori A, et al. (2003). Mouse dexamethasone-induced RAS protein 1 gene is expressed in a circadian rhythmic manner in the suprachiasmatic nucleus. Brain Res. Mol. Brain Res 110, 1–6. 10.1016/s0169-328x(02)00543-0. [PubMed: 12573527]
53. Dause TJ, and Kirby ED (2020). Poor concordance of floxed Sequence recombination in single neural stem cells: implications for cell autonomous studies. eNeuro 7, ENEURO.0470–19.2020. 10.1523/ENEURO.0470-19.2020.
54. Hasegawa S, Fukushima H, Hosoda H, Serita T, Ishikawa R, Rokukawa T, Kawahara-Miki R, Zhang Y, Ohta M, Okada S, et al. (2019). Hippocampal clock regulates memory retrieval via dopamine and PKA-induced GluA1 phosphorylation. Nat. Commun 10, 5766. 10.1038/s41467-019-13554-y. [PubMed: 31852900]
55. Shimizu K, Kobayashi Y, Nakatsuji E, Yamazaki M, Shimba S, Sakimura K, and Fukada Y (2016). SCOP/PHLPP1beta mediates circadian regulation of long-term recognition memory. Nat. Commun 7, 12926. 10.1038/ncomms12926. [PubMed: 27686624]
56. Madar AD, Pfammatter JA, Bordenave J, Plumley EI, Ravi S, Cowie M, Wallace EP, Hermann BP, Maganti RK, and Jones MV (2021). Deficits in behavioral and neuronal pattern separation in temporal lobe epilepsy. J. Neurosci 41, 9669–9686. 10.1523/JNEUROSCI.2439-20.2021. [PubMed: 34620720]
57. Kelly T, and Beck H (2017). Functional properties of granule cells with hilar basal dendrites in the epileptic dentate gyrus. Epilepsia 58, 160–171. 10.1111/epi.13605. [PubMed: 27888509]
58. Karoly PJ, Rao VR, Gregg NM, Worrell GA, Bernard C, Cook MJ, and Baud MO (2021). Cycles in epilepsy. Nat. Rev. Neurol 17, 267–284. 10.1038/s41582-021-00464-1. [PubMed: 33723459]
59. Laszczyk AM, Fox-Quick S, Vo HT, Nettles D, Pugh PC, Over-street-Wadiche L, and King GD (2017). Klotho regulates postnatal neurogenesis and protects against age-related spatial memory loss. Neurobiol. Aging 59, 41–54. 10.1016/j.neurobiolaging.2017.07.008. [PubMed: 28837861]

Highlights

- Dentate neurons exhibit a 24-h oscillation of intrinsic excitability and spiking
- Low excitability during the Light phase results from inhibitory G-protein signaling
- Conditional *Bmal1* deletion increases excitability and spatial discrimination
- *Bmal1* deletion disrupts G-protein regulation of membrane leak currents

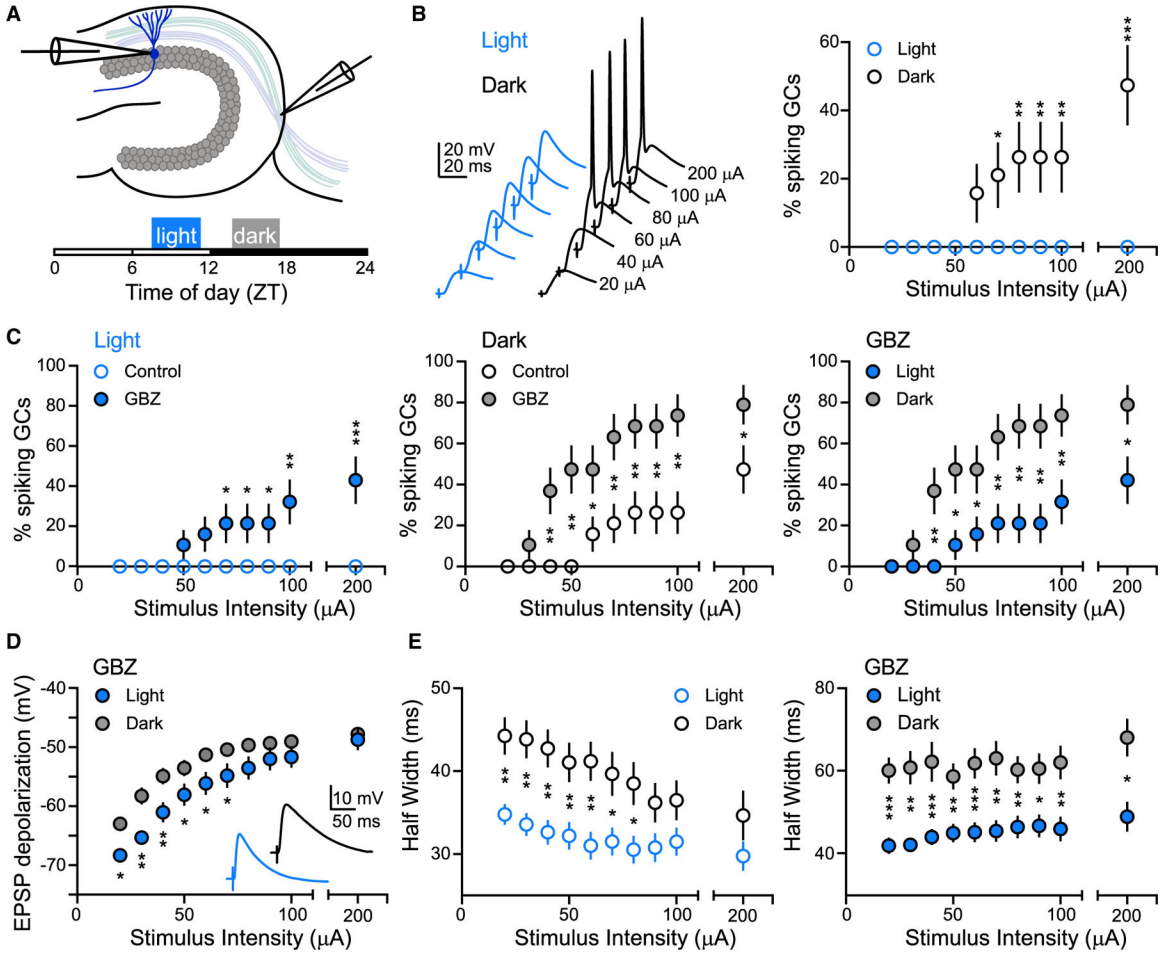

Figure 1. Reduced recruitment of GCs during the Light phase compared to the Dark phase

(A) Current-clamp recordings (I = 0) in response to stimulation of the perforant path were compared in two recording windows: ZT 8–11 (Light) and ZT 14–17 (Dark).

(B) Left, example EPSPs at increasing stimulus intensities. Right, the percentage of GCs recruited to spike was reduced during the Light phase.

(C) Gabazine (GBZ; 10 µM) increased spiking during both the Light (left) and Dark (middle) phases. Right, GBZ, a smaller percentage of GCs were recruited during the Light. (B and C) χ^2 tests, *p < 0.05; **p < 0.01; ***p < 0.001.

(D) Depolarization by subthreshold EPSPs was reduced during the Light (in GBZ). Inset, EPSPs evoked at 100 µA.

(E) EPSP half-widths were reduced during the Light in control (left) and GBZ (right). (D and E) Multiple unpaired t test comparison by the Holm-Sidak method.

*p < 0.05; **p < 0.01; ***p < 0.001. (B–E) n = 19, 19. Symbols represent mean ± SEM.

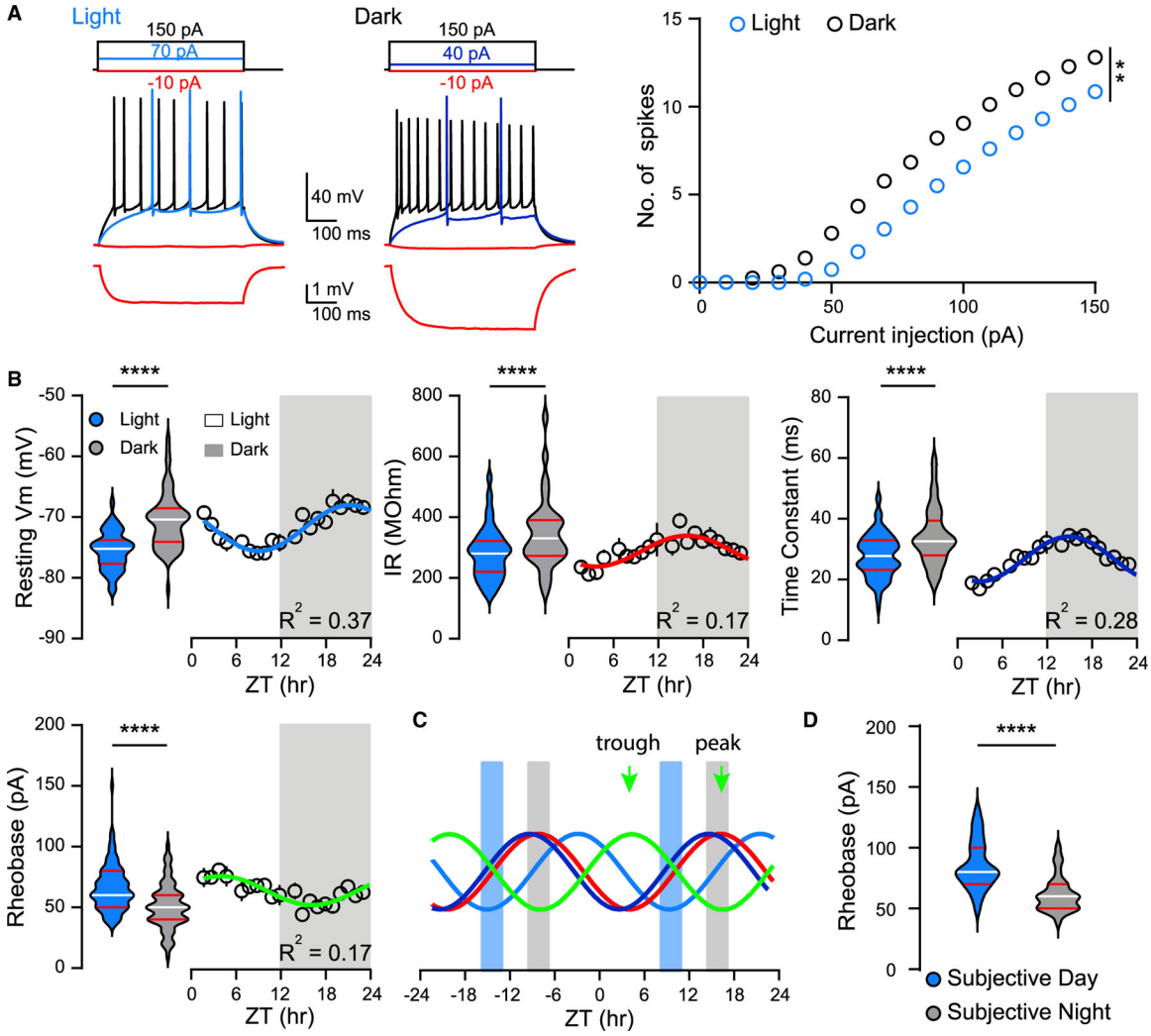

Figure 2. Reduced intrinsic excitability during the Light phase

(A) Left, examples of current injections (top) used to measure GC intrinsic properties (bottom). Right, number of spikes elicited by current steps revealed reduced spiking during the Light phase. n = 90 (Light); 69 (Dark). Unpaired t test to compare area under the curve (AUC) t = 2.9 **p < 0.01.

(B) Violin plots show RMP, IR, TC, and rheobase during the Light (blue) and Dark (gray) phases. Mann-Whitney *U* test, *U* = 1,141 (RMP), U = 1,997 (IR), U = 1,845 (TC), and unpaired t test, t = 5.1 (rheobase). ****p < 0.0001. n = 90 (Light); 69 (Dark). Dot plots show intrinsic properties averaged in 1-h bins fit with Cosinor function across 24 h. Lights on at ZT0 and off at ZT12. n = 9–39 cells per bin.

(C) Overlay of Cosinor fits for intrinsic properties, normalized in amplitude (same color code as in B). Blue and gray bars denote the Light and Dark recording windows, respectively. Arrows point to trough and peak of excitability based on acrophase for rheobase.

(D) Violin plots show rheobase recorded at Subjective Day (Circadian Time or CT 8–11, where CT 12 refers to activity onset) and Subjective Night (CT 14–17) from mice housed

in constant dark. Unpaired t test, t = 5 ****p < 0.0001. n = 27, 27. Bars on violin plots represent quartile and median values. Symbols represent mean ± SEM.

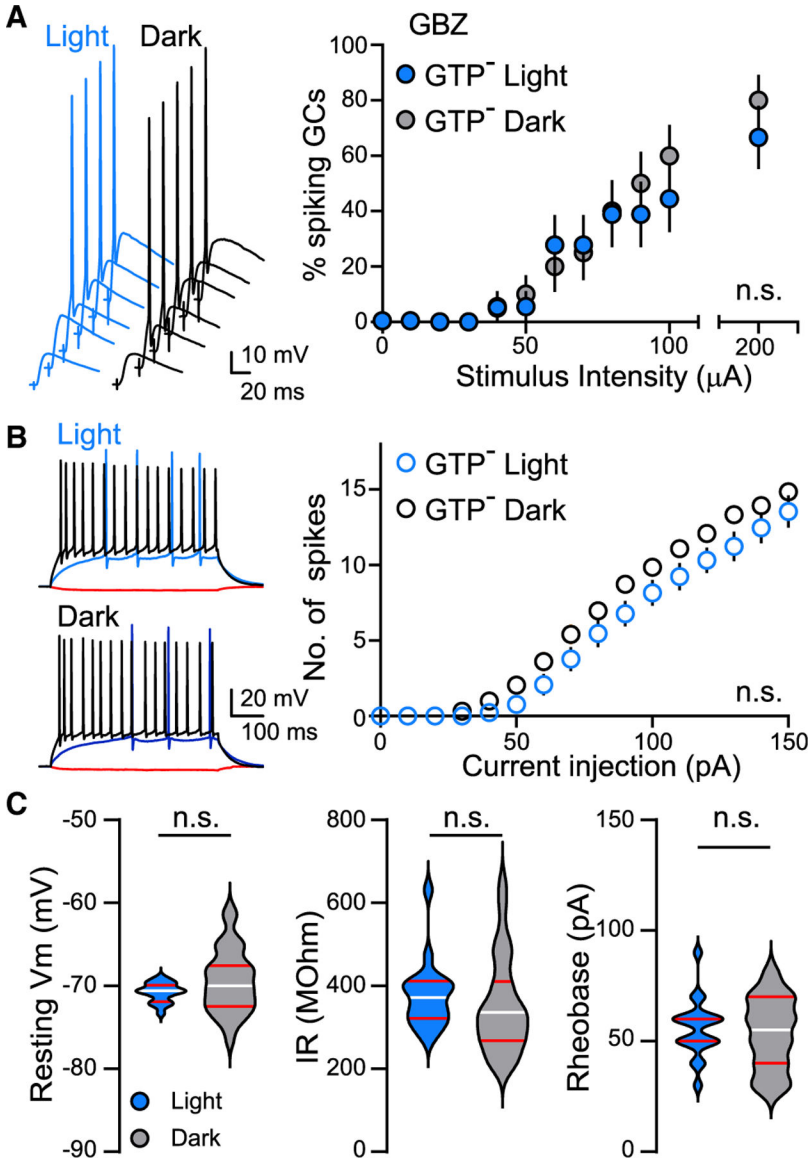

Figure 3. Diurnal regulation of excitability requires intracellular GTP

(A) Left, example EPSPs at increasing stimulus intensities (as in Figure 1) in the absence of Na-GTP (GTP^{-}) in the recording pipette. Right, the percentage of GCs recruited to spike by perforant path stimulation was similar during the Light and Dark phases; χ^2 tests $p > 0.05$ at all stimulus intensities.

(B) Left, example voltage traces in response to somatic current injections of −10 pA (red), rheobase (blue), and 150 pA (black). Right, the number of spikes elicited by current steps was similar during the Light and Dark phases. Unpaired t test to compare area under the curve (AUC) $t = 0.78$; $p = 0.44$.

(C) Intrinsic properties in the absence of GTP were similar between Light and Dark phases for RMP (left; Mann-Whitney *U* test, $U = 212$; $p = 0.24$), IR (middle; unpaired t test, $t = 0.94$; $p = 0.35$), and rheobase (right; unpaired t test, $t = 0.5$; $p = 0.61$). (A–C) n = 19 Light

and 28 Dark. Bars on violin plots represent quartile and median values. Symbols represent mean ± SEM.

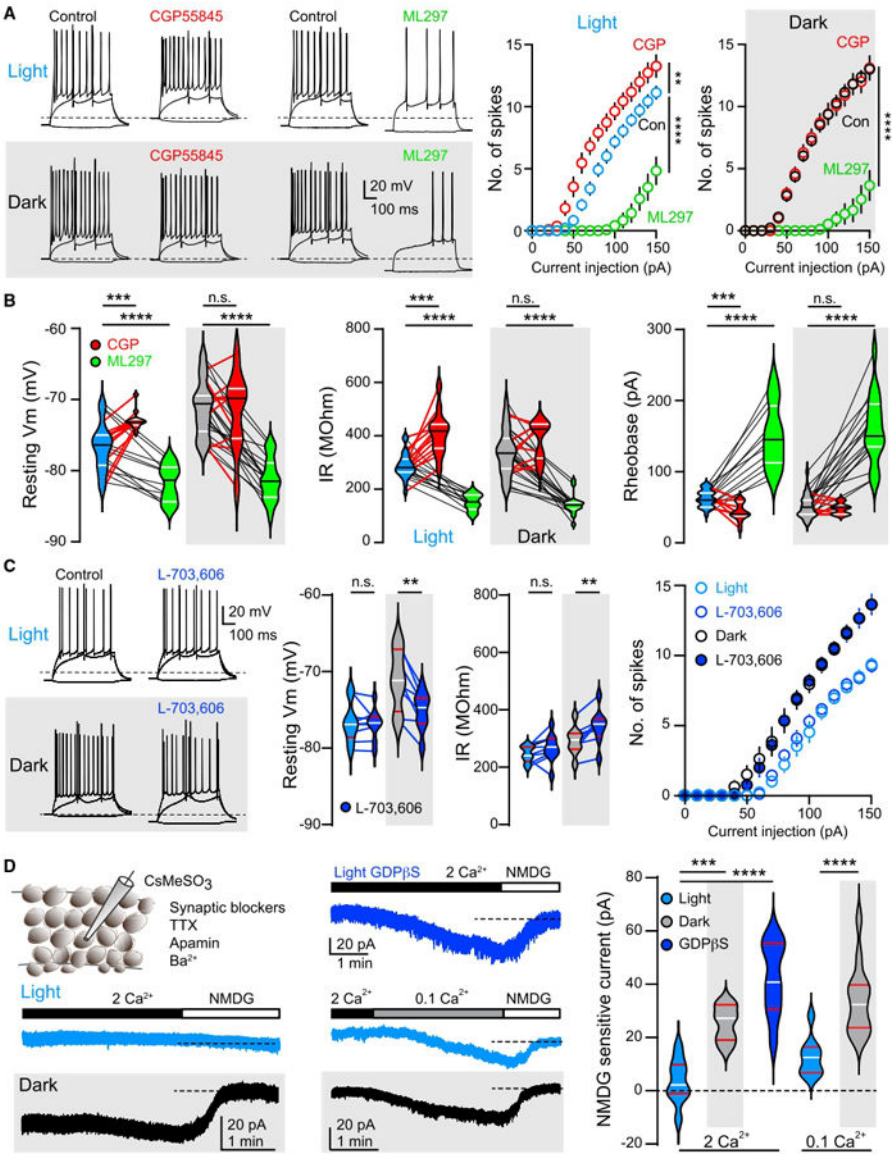

Figure 4. Diurnal regulation of G-protein gated K^+ and Na^+ conductances

(A) Left, example voltage traces in response to current injections (−10 pA, rheobase and +150 pA) in CGP55845 (10 μM; red) or ML297 (10 μM; green) during Light (top) or Dark phases (bottom). Dotted line indicates −70 mV. Right, the number of action potentials elicited by current injections in the same conditions. Controls for application of CGP and ML297 (a paired analysis) were pooled. In Light, n = 11 for CGP, n = 12 for ML297. In Dark, n = 10 for CGP, n = 17 for ML297. One-way ANOVA to compare area under the curve (AUC) $F_{(2,43)} = 46.9$ and $F_{(2,51)} = 65.2$ for Light and Dark, respectively, followed by Tukey's multiple comparisons test. **p < 0.01; ****p < 0.0001.

(B) Violin plots showing effects of CGP55845 (red) or ML297 (green) during the Light and Dark phases. For RMP in Light, CGP paired t test t = 5.6; ML297 t = 7.1. In Dark, CGP t = 0.2; ML297 t = 10.3. For IR in Light, CGP paired t test t = 6.1; ML297 t = 8.9. In Dark,

CGP t = 1.7; ML297 t = 8.7. For rheobase in Light, CGP paired t test t = 5.5; ML297 t = 8.1. In Dark, CGP t = 0.0; ML297 t = 9.7. n.s. $p > 0.05$; ***$p < 0.001$; ****$p < 0.0001$.
(C) Left, example voltage traces in response to current injections (−10 pA, rheobase and +150 pA) in L-703,606 (10 μM; dark blue) during Light (top) or Dark phases (bottom). Dotted line indicates −70 mV. Middle, violin plots showing effects of L-703,606 during the Light and Dark phases. For RMP in Light, L-703,606 paired t test t = 0.5; p = 0.57, in Dark t = 4.8. For IR in Light, paired t test t = 1.6; p = 0.13, in Dark t = 4. **$p < 0.01$; n = 9, 9. Right, the number of action potentials elicited by current injections. Unpaired t test to compare area under the curve (AUC) t = 1.6; p = 0.11 and t = 0.8; p = 0.41 for Light and Dark, respectively.
(D) Left, examples of isolated Na^+ leak currents at −70 mV during the Light (blue) or Dark (gray) phases. Dashed line indicates the current blocked by NMDG in each condition. Right, violin plots show larger NMDG-sensitive Na^+ currents during the Dark phase and in presence of GDPβS during Light phase. Unpaired t test in 2 mM Ca^{2+}, t = 5.6; in 0.1 mM Ca^{2+}, t = 4.5; GDPβS unpaired t test against Light 2 mM Ca^{2+}, t = 5.9. ***$p < 0.001$; ****$p < 0.0001$. n = 9, 7, 9, 13, and 4 for Light 2 mM Ca^{2+}, Dark 2 mM Ca^{2+}, Light 0.1 mM Ca^{2+}, Dark 0.1 mM Ca^{2+}, and Light GDPβS, respectively. Bars on violin plots represent quartile and median values. Symbols represent mean ± SEM.

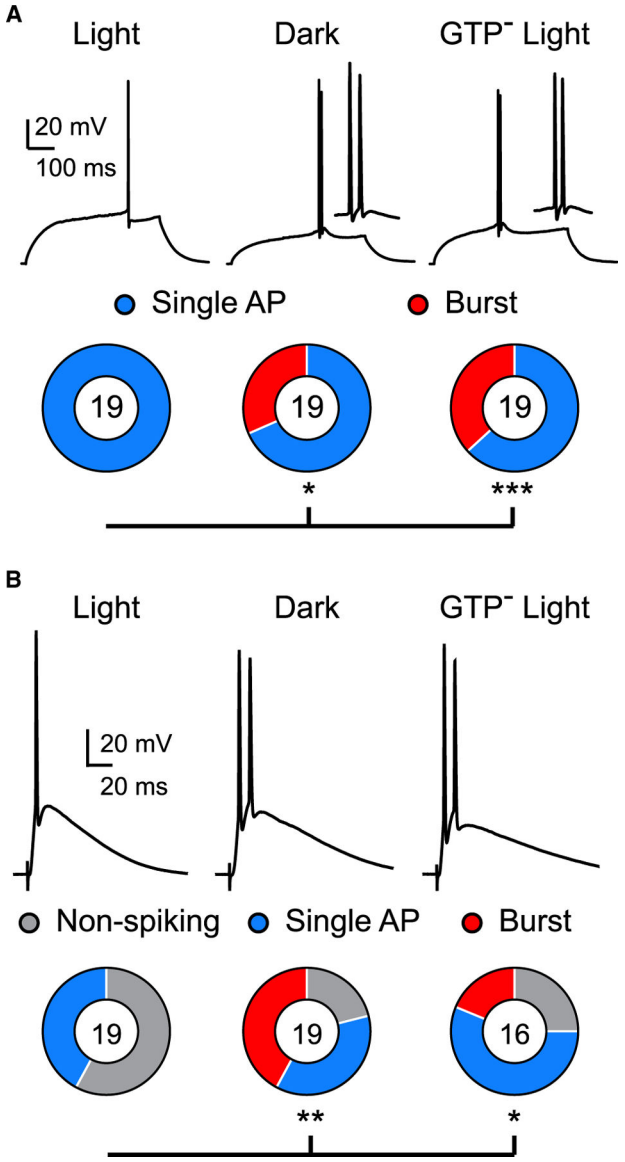

Figure 5. GTP-dependent diurnal regulation of spike bursts

(A) Example voltage traces in response to rheobase current injection during the Light phase (left), Dark phase (middle), and Light phase using a GTP^{-} internal (right). Insets show enlargement of the action potentials (APs). Sectors represent the fraction of GCs with single or multiple APs in each condition (χ^2 tests, *p < 0.05; ***p < 0.001).

(B) Examples of APs evoked in response to perforant path stimulation at 200 μA in GBZ. Sectors represent the percentage of GCs with each spike pattern, as well as non-spiking cells. χ^2 tests, *p < 0.05; **p < 0.01. No. of cells is indicated.

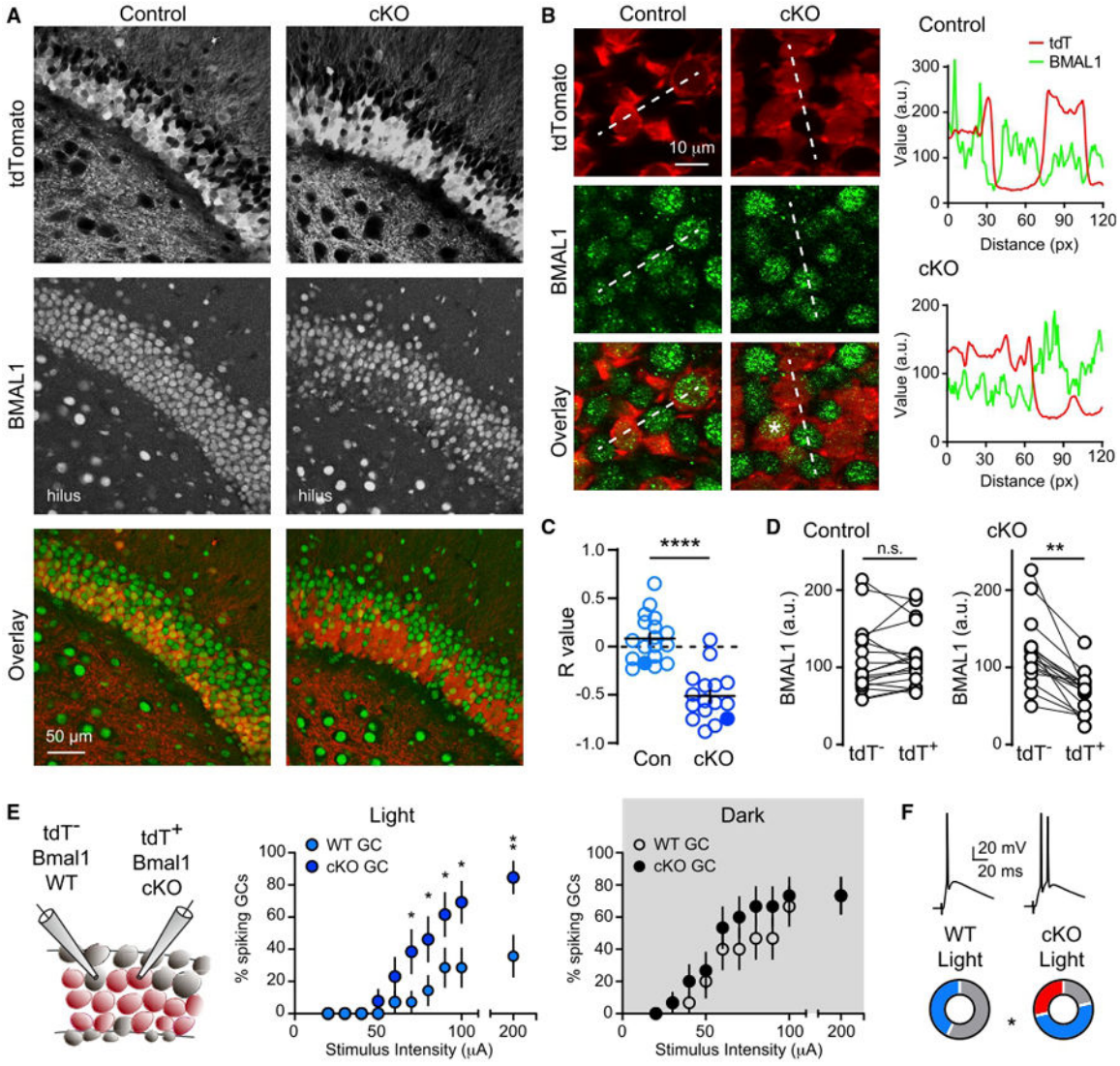

Figure 6. Diurnal regulation of synaptic recruitment is disrupted by *Bmal1* cKO

(A) Low-magnification confocal images from *Pomc-Cre*:*tdT* (control) and *Pomc-Cre*:*tdT*:*Bmal1*$^{lox/lox}$ (cKO) mice showing BMAL1 immunolabeling.

(B) Left, high-magnification images from control or cKO mice. Dashed lines show regions of interest (ROIs) where fluorescence was measured in arbitrary units (a.u.). *Highlights a tdT^{+} cell without *Bmal1* deletion (see discussion). Right, examples of fluorescence measures from ROIs in the indicated channels.

(C) R values show a negative correlation for tdT and Bmal1 only in cKOs. Filled symbols represent examples in (B). Unpaired t test t = 5.4. ****p < 0.0001.

(D) BMAL1 levels in tdT^{-} and tdT^{+} neighboring cells in control and cKO mice. Paired t test t = 0.5; p = 0.58 and t = 5.8 for control and cKO, respectively. **p < 0.01. n = 18, 16 ROIs from three control and six cKO mice.

(E) Schematic of recording from neighboring WT (tdT^{-}) and cKO (tdT^{+}) GCs. A greater fraction of cKO GCs compared with WT GCs spiked in response to perforant path

stimulation in the Light phase (left, n = 14 pairs of GCs) but not in the Dark phase (right, n = 15 pairs of GCs).

(F) *Bmal1* cKO GCs exhibited burst firing in response to perforant path stimulation during Light phase. Sectors represent non-spiking (gray), single spikes (blue), and burst firing patterns (red). n = 14 pairs of GCs. (E and F) χ^2 tests, *p < 0.05; **p < 0.01. Symbols represent mean ± SEM.

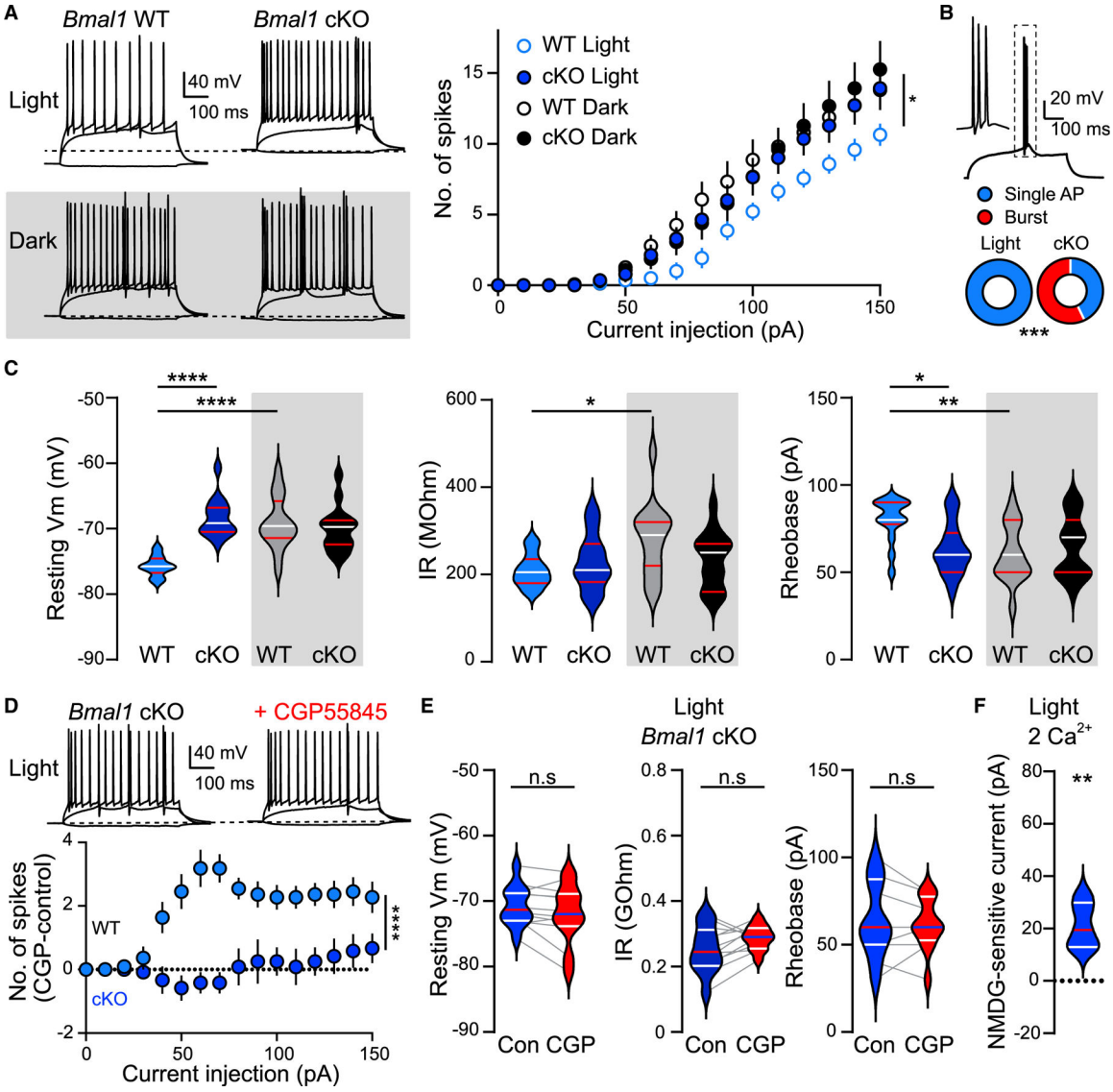

Figure 7. Diurnal regulation of intrinsic excitability is disrupted by *Bmal1* Cko

(A) Left, examples of voltage traces in response to current injections (of −10 pA, rheobase, and 150 pA) for tdT^{-} (WT) and tdT^{+} (cKO) GCs. Dashed line marks avg RMP during the Dark phase. Right, number of APs elicited by current injections in the same conditions, blue symbols denote Light phase and black denotes Dark phase. Welch's ANOVA to compare area under the curve (AUC) $F_{(3,28)} = 3.44$ followed by Dunnett's multiple comparisons test. *p < 0.05.

(B) *Bmal1* cKO GCs exhibited burst firing during the Light phase. Sectors represent differences in discharge profile. χ^2 tests, ***p < 0.001. n = 14 pairs of WT and cKO GCs.

(C) Intrinsic properties of WT and cKO GCs during the Light (blue) and Dark (black) phases. One-way ANOVA for RMP ($F_{(3,54)} = 16.24$), IR ($F_{(3,54)} = 3.06$), and rheobase ($F_{(3,54)} = 4.52$) followed by Tukey's multiple comparison test. *p < 0.05; **p < 0.01; ****p < 0.0001. (A–C) Sample size n = 14 pairs in the Light phase, n = 15 in the Dark phase.

(D) Top, example voltage traces before and after application of GCP55845 (10 μM; CGP) in a cKO GC in the Light phase. Dashed line marks avg RMP during the Dark phase. Bottom, comparison of the additional number of action potentials elicited by CGP (CGP – control) in Bmal1 WT and *Bmal1* cKO GCs in the Light phase. Unpaired t test to compare area under the curve (AUC) $t = 5.1$; ****$p < 0.0001$.

(E) Violin plots of intrinsic properties from *Bmal1* cKO GCs show that CGP had no effect during the Light phase. Paired t test for RMP ($t = 1.9$), IR ($t = 2$), and rheobase ($t = 0.8$); $p > 0.05$. $n = 12$.

(F) Violin plot showing a robust NMDG-sensitive current in *Bmal1* cKO GCs in the Light phase (contrast with Figure 4C). Unpaired t test $t = 3.7$. **$p < 0.01$. $n = 5$. Bars on violin plots represent quartile and median values. Symbols represent mean ± SEM.

Cell Rep. Author manuscript; available in PMC 2023 October 23.

KEY RESOURCES TABLE

REAGENT or RESOURCE	SOURCE	IDENTIFIER
Antibodies		
Rabbit anti-BMAL1	Novus Biologicals	Novus Cat# NB100–2288; RRID:AB_10000794
Goat anti-rabbit Alexa Fluor 488	Thermo Fisher Scientific	Thermo Fisher Cat#A11008; RRID:AB_143165
Goat anti h-Prox1	R&D Systems	R&D Systems Cat# AF2727; RRID:AB_2170716
Donkey anti-goat Flexa Fluor 647	Thermo Fisher Scientific	ThermoFisher Cat#A21447; RRID:AB_2535864
Chemicals, peptides, and recombinant proteins		
SR95531 (Gabazine)	Abcam	ab120042
CGP55845	Abcam	ab120337
ML297	Sigma-Aldrich	SML0836
L-703,606	Sigma-Aldrich	L119
NBQX	Abcam	ab120045
(R)-CPP	Abcam	ab120159
Tetrodotoxin citrate	Abcam	ab120054
Picrotoxin	Abcam	ab120315
Apamin	Tocris	Cat No 1652
Experimental models: Organisms/strains		
Mouse/C57BL/6J	JAX	Jackson#000664; RRID:IMSR_JAX:000664
Mouse/PV-Cre	JAX	Jackson#017320;RRID:IMSR_JAX:017320
Mouse/nNOS-CreERt2	JAX	Jackson#014541; RRID:IMSR_JAX:014541
Mouse/Ai14	JAX	Jackson#007914;RRID:IMSR_JAX:007914
Mouse/Ai32	JAX	Jackson#024109;RRID:IMSR_JAX:024109
Mouse/Pomc-Cre	JAX	Jackson#010714;RRID:IMSR_JAX:010714
Mouse/Bmal1 lox	JAX	Jackson#007668; RRID:IMSR_JAX:007668
Software and algorithms		
PClamp	Molecular Devices	v.10.7.0.3
Clampfit	Molecular Devices	v.10.7.0.3

REAGENT or RESOURCE	SOURCE	IDENTIFIER
Axograph X	Axograph Scientific	v.1.7.6
Prism	GraphPad Software	v.9.2.0
SPSS	IBM	v.25
ImageJ	https://imagej.nih.gov	1.8.0_172
TopScan	CleverSys	v. 2.0
ClockLab	Actimetrics	v.6